



**AFRL-RX-WP-TP-2014-0080**

**MECHANISMS RELATED TO DIFFERENT  
GENERATIONS OF  $\gamma'$  PRECIPITATION DURING  
CONTINUOUS COOLING OF A NICKEL BASE  
SUPERALLOY (POSTPRINT)**

**J. Tiley and G.B. Viswanathan  
AFRL/RXCM**

**APRIL 2012  
Interim Report**

**Approved for public release; distribution unlimited.**

*See additional restrictions described on inside pages*

**STINFO COPY**

**© 2012 Elsevier Ltd.**

**AIR FORCE RESEARCH LABORATORY  
MATERIALS AND MANUFACTURING DIRECTORATE  
WRIGHT-PATTERSON AIR FORCE BASE, OH 45433-7750  
AIR FORCE MATERIEL COMMAND  
UNITED STATES AIR FORCE**

## NOTICE AND SIGNATURE PAGE

Using Government drawings, specifications, or other data included in this document for any purpose other than Government procurement does not in any way obligate the U.S. Government. The fact that the Government formulated or supplied the drawings, specifications, or other data does not license the holder or any other person or corporation; or convey any rights or permission to manufacture, use, or sell any patented invention that may relate to them.

This report was cleared for public release by the USAF 88th Air Base Wing (88 ABW) Public Affairs Office (PAO) and is available to the general public, including foreign nationals.

Copies may be obtained from the Defense Technical Information Center (DTIC)  
(<http://www.dtic.mil>).

AFRL-RX-WP-TP-2014-0080 HAS BEEN REVIEWED AND IS APPROVED FOR  
PUBLICATION IN ACCORDANCE WITH ASSIGNED DISTRIBUTION STATEMENT.

//Signature//

---

JAIMIE TILEY, Project Engineer  
Metals Branch  
Structural Materials Division

//Signature//

---

DANIEL EVANS, Chief  
Metals Branch  
Structural Materials Division

//Signature//

---

ROBERT T. MARSHALL, Deputy Chief  
Structural Materials Division  
Materials and Manufacturing Directorate

This report is published in the interest of scientific and technical information exchange, and its publication does not constitute the Government's approval or disapproval of its ideas or findings.

| REPORT DOCUMENTATION PAGE                                                                                                                                                                                                                                                                                                                                                                                                                                                                                                                                                                                                                                                                                                                                                                                                                                                                                                                                                                                                                                                                                                                                                                                                                                                                                                                                                                                                                                                                                                                                                                                                                                                                                       |                             |                              |                                        | Form Approved<br>OMB No. 0704-0188                                           |                                                             |
|-----------------------------------------------------------------------------------------------------------------------------------------------------------------------------------------------------------------------------------------------------------------------------------------------------------------------------------------------------------------------------------------------------------------------------------------------------------------------------------------------------------------------------------------------------------------------------------------------------------------------------------------------------------------------------------------------------------------------------------------------------------------------------------------------------------------------------------------------------------------------------------------------------------------------------------------------------------------------------------------------------------------------------------------------------------------------------------------------------------------------------------------------------------------------------------------------------------------------------------------------------------------------------------------------------------------------------------------------------------------------------------------------------------------------------------------------------------------------------------------------------------------------------------------------------------------------------------------------------------------------------------------------------------------------------------------------------------------|-----------------------------|------------------------------|----------------------------------------|------------------------------------------------------------------------------|-------------------------------------------------------------|
| <p>The public reporting burden for this collection of information is estimated to average 1 hour per response, including the time for reviewing instructions, searching existing data sources, gathering and maintaining the data needed, and completing and reviewing the collection of information. Send comments regarding this burden estimate or any other aspect of this collection of information, including suggestions for reducing this burden, to Department of Defense, Washington Headquarters Services, Directorate for Information Operations and Reports (0704-0188), 1215 Jefferson Davis Highway, Suite 1204, Arlington, VA 22202-4302. Respondents should be aware that notwithstanding any other provision of law, no person shall be subject to any penalty for failing to comply with a collection of information if it does not display a currently valid OMB control number. <b>PLEASE DO NOT RETURN YOUR FORM TO THE ABOVE ADDRESS.</b></p>                                                                                                                                                                                                                                                                                                                                                                                                                                                                                                                                                                                                                                                                                                                                            |                             |                              |                                        |                                                                              |                                                             |
| 1. REPORT DATE (DD-MM-YY)<br>April 2012                                                                                                                                                                                                                                                                                                                                                                                                                                                                                                                                                                                                                                                                                                                                                                                                                                                                                                                                                                                                                                                                                                                                                                                                                                                                                                                                                                                                                                                                                                                                                                                                                                                                         |                             | 2. REPORT TYPE<br>Interim    |                                        | 3. DATES COVERED (From - To)<br>01 December 2009 – 31 March 2012             |                                                             |
| 4. TITLE AND SUBTITLE<br>MECHANISMS RELATED TO DIFFERENT GENERATIONS OF $\gamma'$ PRECIPITATION DURING CONTINUOUS COOLING OF A NICKEL BASE SUPERALLOY (POSTPRINT)                                                                                                                                                                                                                                                                                                                                                                                                                                                                                                                                                                                                                                                                                                                                                                                                                                                                                                                                                                                                                                                                                                                                                                                                                                                                                                                                                                                                                                                                                                                                               |                             |                              |                                        | 5a. CONTRACT NUMBER<br>In-house                                              |                                                             |
|                                                                                                                                                                                                                                                                                                                                                                                                                                                                                                                                                                                                                                                                                                                                                                                                                                                                                                                                                                                                                                                                                                                                                                                                                                                                                                                                                                                                                                                                                                                                                                                                                                                                                                                 |                             |                              |                                        | 5b. GRANT NUMBER                                                             |                                                             |
|                                                                                                                                                                                                                                                                                                                                                                                                                                                                                                                                                                                                                                                                                                                                                                                                                                                                                                                                                                                                                                                                                                                                                                                                                                                                                                                                                                                                                                                                                                                                                                                                                                                                                                                 |                             |                              |                                        | 5c. PROGRAM ELEMENT NUMBER<br>62102F                                         |                                                             |
| 6. AUTHOR(S)<br>J. Tiley and G.B. Viswanathan (AFRL/RXCM)<br>See back.                                                                                                                                                                                                                                                                                                                                                                                                                                                                                                                                                                                                                                                                                                                                                                                                                                                                                                                                                                                                                                                                                                                                                                                                                                                                                                                                                                                                                                                                                                                                                                                                                                          |                             |                              |                                        | 5d. PROJECT NUMBER<br>4347                                                   |                                                             |
|                                                                                                                                                                                                                                                                                                                                                                                                                                                                                                                                                                                                                                                                                                                                                                                                                                                                                                                                                                                                                                                                                                                                                                                                                                                                                                                                                                                                                                                                                                                                                                                                                                                                                                                 |                             |                              |                                        | 5e. TASK NUMBER                                                              |                                                             |
|                                                                                                                                                                                                                                                                                                                                                                                                                                                                                                                                                                                                                                                                                                                                                                                                                                                                                                                                                                                                                                                                                                                                                                                                                                                                                                                                                                                                                                                                                                                                                                                                                                                                                                                 |                             |                              |                                        | 5f. WORK UNIT NUMBER<br>X0DE                                                 |                                                             |
| 7. PERFORMING ORGANIZATION NAME(S) AND ADDRESS(ES)<br>AFRL/RXCM<br>2941 Hobson Way<br>Wright-Patterson AFB OH 45433-7817                                                                                                                                                                                                                                                                                                                                                                                                                                                                                                                                                                                                                                                                                                                                                                                                                                                                                                                                                                                                                                                                                                                                                                                                                                                                                                                                                                                                                                                                                                                                                                                        |                             |                              |                                        | See back.                                                                    |                                                             |
| 9. SPONSORING/MONITORING AGENCY NAME(S) AND ADDRESS(ES)<br>Air Force Research Laboratory<br>Materials and Manufacturing Directorate<br>Wright-Patterson Air Force Base, OH 45433-7750<br>Air Force Materiel Command<br>United States Air Force                                                                                                                                                                                                                                                                                                                                                                                                                                                                                                                                                                                                                                                                                                                                                                                                                                                                                                                                                                                                                                                                                                                                                                                                                                                                                                                                                                                                                                                                  |                             |                              |                                        | 10. SPONSORING/MONITORING AGENCY ACRONYM(S)<br>AFRL/RXCM                     |                                                             |
|                                                                                                                                                                                                                                                                                                                                                                                                                                                                                                                                                                                                                                                                                                                                                                                                                                                                                                                                                                                                                                                                                                                                                                                                                                                                                                                                                                                                                                                                                                                                                                                                                                                                                                                 |                             |                              |                                        | 11. SPONSORING/MONITORING AGENCY REPORT NUMBER(S)<br>AFRL-RX-WP-TP-2014-0080 |                                                             |
| 12. DISTRIBUTION/AVAILABILITY STATEMENT<br>Approved for public release; distribution unlimited.                                                                                                                                                                                                                                                                                                                                                                                                                                                                                                                                                                                                                                                                                                                                                                                                                                                                                                                                                                                                                                                                                                                                                                                                                                                                                                                                                                                                                                                                                                                                                                                                                 |                             |                              |                                        |                                                                              |                                                             |
| 13. SUPPLEMENTARY NOTES<br>PA Case Number: 88ABW-2012-2971 ; Clearance Date: 21 May 2012. Journal article published in <i>Acta Materialia</i> , Vol 61, 2013, pp. 280-293. © 2012 Elsevier Ltd. The U.S. Government is joint author of the work and has the right to use, modify, reproduce, release, perform, display, or disclose the work. This document contains color. The final publication is available at <a href="http://www.sciencedirect.com">www.sciencedirect.com</a>                                                                                                                                                                                                                                                                                                                                                                                                                                                                                                                                                                                                                                                                                                                                                                                                                                                                                                                                                                                                                                                                                                                                                                                                                              |                             |                              |                                        |                                                                              |                                                             |
| 14. ABSTRACT (Maximum 200 words)<br>This paper focuses on developing a mechanistic understanding of the process of multiple nucleation bursts leading to the formation of multiple generations (or populations) of $\gamma'$ precipitates with different size distributions, during the continuous cooling of a commercially used nickel base superalloy. This mechanistic understanding has been developed based on a number of critical experimental results: direct observation of the multiple nucleation bursts during in situ X-ray diffraction studies in the synchrotron, characterization of the size distributions associated with the different populations of $\gamma'$ precipitates by coupling multiple imaging techniques at the appropriate length scale and detailed compositional analysis of the $\gamma'$ precipitates as well as the c matrix using atom probe tomography. These analyses reveal that while local compositional equilibrium appears to have been achieved near the $\gamma'/\gamma$ interface for the first generation of precipitates, a non-equilibrium long range diffusion profile in the c matrix is retained during the process of continuous cooling, which is largely responsible for the subsequent nucleation bursts at larger undercooling (or lower temperatures), leading to second and third generations of precipitates. Additionally, since these subsequent generations of precipitates are formed at larger undercoolings, they are typically finer in size scale, exhibit far-from equilibrium compositions and also have very diffuse $\gamma'/\gamma$ interfaces, indicating a non-classical precipitation mechanism associated with their formation. |                             |                              |                                        |                                                                              |                                                             |
| 15. SUBJECT TERMS<br>nickel based superalloy, Rene 88 DT; generations, nucleation, spinodal decomposition, atom probe tomography, EFTEM                                                                                                                                                                                                                                                                                                                                                                                                                                                                                                                                                                                                                                                                                                                                                                                                                                                                                                                                                                                                                                                                                                                                                                                                                                                                                                                                                                                                                                                                                                                                                                         |                             |                              |                                        |                                                                              |                                                             |
| 16. SECURITY CLASSIFICATION OF:                                                                                                                                                                                                                                                                                                                                                                                                                                                                                                                                                                                                                                                                                                                                                                                                                                                                                                                                                                                                                                                                                                                                                                                                                                                                                                                                                                                                                                                                                                                                                                                                                                                                                 |                             |                              | 17. LIMITATION OF ABSTRACT:<br><br>SAR | 18. NUMBER OF PAGES<br><br>18                                                | 19a. NAME OF RESPONSIBLE PERSON (Monitor)<br>Jaimie Tiley   |
| a. REPORT<br>Unclassified                                                                                                                                                                                                                                                                                                                                                                                                                                                                                                                                                                                                                                                                                                                                                                                                                                                                                                                                                                                                                                                                                                                                                                                                                                                                                                                                                                                                                                                                                                                                                                                                                                                                                       | b. ABSTRACT<br>Unclassified | c. THIS PAGE<br>Unclassified |                                        |                                                                              | 19b. TELEPHONE NUMBER (Include Area Code)<br>(937) 255-7416 |

## REPORT DOCUMENTATION PAGE Cont'd

### 6. AUTHOR(S)

A.R.P. Singh, S. Nag, and R. Banerjee, University of North Texas  
S. Chattopadhyay, Argonne National Laboratory and Illinois Institute of Technology  
Y. Ren, Argonne National Laboratory  
H.L. Fraser, The Ohio State University

### 7. PERFORMING ORGANIZATION NAME(S) AND ADDRESS(ES)

University of North Texas  
1155 Union Circle  
Denton, TX 76203-5017

Argonne National Laboratory  
9700 S. Cass Avenue  
Argonne, IL 60439

Illinois Institute of Technology  
3300 South Federal Street  
Chicago, IL 60616-3793

The Ohio State University  
281 West Lane Avenue  
Columbus, OH 43210

# Mechanisms related to different generations of $\gamma'$ precipitation during continuous cooling of a nickel base superalloy

A.R.P. Singh<sup>a</sup>, S. Nag<sup>a</sup>, S. Chattopadhyay<sup>b,c</sup>, Y. Ren<sup>f</sup>, J. Tiley<sup>d</sup>, G.B. Viswanathan<sup>d</sup>,  
H.L. Fraser<sup>e</sup>, R. Banerjee<sup>a,\*</sup>

<sup>a</sup> Center for Advanced Research and Technology and Department of Materials Science and Engineering, University of North Texas, Denton, TX, USA

<sup>b</sup> CSRRI-IIT, MRCAT, Advanced Photon Source, Argonne National Laboratory, 9700 S. Cass Avenue, Argonne, IL 60439, USA

<sup>c</sup> Physics Department, Illinois Institute of Technology, Chicago, IL 60616, USA

<sup>d</sup> Materials and Manufacturing Directorate, Air Force Research Laboratory, Dayton, OH, USA

<sup>e</sup> Center for the Accelerated Maturation of Materials and Department of Materials Science and Engineering, The Ohio State University, Columbus, OH, USA

<sup>f</sup> X-ray Science Division, Advanced Photon Source, Argonne National Laboratory, 9700 S. Cass Avenue, Argonne, IL 60439, USA

Received 10 May 2012; received in revised form 18 September 2012; accepted 22 September 2012

Available online 22 October 2012

## Abstract

This paper focuses on developing a mechanistic understanding of the process of multiple nucleation bursts leading to the formation of multiple generations (or populations) of  $\gamma'$  precipitates with different size distributions, during the continuous cooling of a commercially used nickel base superalloy. This mechanistic understanding has been developed based on a number of critical experimental results: direct observation of the multiple nucleation bursts during in situ X-ray diffraction studies in the synchrotron, characterization of the size distributions associated with the different populations of  $\gamma'$  precipitates by coupling multiple imaging techniques at the appropriate length scale and detailed compositional analysis of the  $\gamma'$  precipitates as well as the  $\gamma$  matrix using atom probe tomography. These analyses reveal that while local compositional equilibrium appears to have been achieved near the  $\gamma'/\gamma$  interface for the first generation of precipitates, a non-equilibrium long range diffusion profile in the  $\gamma$  matrix is retained during the process of continuous cooling, which is largely responsible for the subsequent nucleation bursts at larger undercooling (or lower temperatures), leading to second and third generations of precipitates. Additionally, since these subsequent generations of precipitates are formed at larger undercoolings, they are typically finer in size scale, exhibit far-from equilibrium compositions and also have very diffuse  $\gamma'/\gamma$  interfaces, indicating a non-classical precipitation mechanism associated with their formation.

© 2012 Acta Materialia Inc. Published by Elsevier Ltd. All rights reserved.

**Keywords:** Nickel base superalloy; Rene 88 DT; Generations, Nucleation; Spinodal decomposition; Atom probe tomography; EFTEM

## 1. Introduction

Nickel base superalloys possess an excellent balance of properties like high strength, ductility, fracture toughness and good fatigue and corrosion resistance, at both room temperature and elevated temperatures. Due to these unique properties they have widespread application in a number of critical technological areas, especially those involving high temperatures such as aircraft jet engines.

These properties in nickel base superalloys arise by the precipitation of the ordered  $\gamma'$  phase (in some cases both  $\gamma'$  and  $\gamma''$  phases) within a disordered  $\gamma$  matrix. The microstructure of these alloys, especially in terms of the composition, morphology and spatial and size distributions of the  $\gamma'$  precipitates, plays a very important role in determining the mechanical properties of these alloys [1,2]. Rene 88 DT alloy, a recently developed nickel base superalloy [3–5], exhibits better mechanical properties than the previous-generation Rene 95 alloy, such as improved creep strength and fatigue crack growth resistance [5]. The nominal chemistry for this alloy is: 13% Co, 16% Cr, 4% Mo, 4% W, 2.1%

\* Corresponding author. Tel.: +1 940 891 6812; fax: +1 940 565 4824.  
E-mail address: [rajarshi.banerjee@unt.edu](mailto:rajarshi.banerjee@unt.edu) (R. Banerjee).

Al, 3.7% Ti, 0.7% Nb, 0.03% C, 0.015% B and balance Ni. This alloy is typically processed through the powder metallurgy route and develops a polycrystalline microstructure consisting of  $\gamma$  grains with nanoscale  $\gamma'$  precipitates. Furthermore, the typical heat treatment used for this alloy consists of a solutionizing procedure for 30 to 60 min at 1150 °C (2100 °F) in the single  $\gamma$  phase field, followed by continuous cooling to room temperature at appropriate cooling rates, and subsequent aging for different time periods at temperatures such as 760 °C (1400 °F).

The microstructural evolution in superalloys such as Rene 88 DT, during continuous cooling, is strongly dependent on the cooling rate employed. Faster cooling rates, such as those encountered during water quenching the alloy from the high temperature single  $\gamma$  phase field, typically lead to the formation of a monomodal size distribution of refined  $\gamma'$  precipitates [6–8]. In contrast, relatively slower cooling rates lead to the formation of  $\gamma'$  precipitates with a bimodal size distribution or in some cases even a multimodal size distribution [6,9–13]. The development of multiple populations of  $\gamma'$  precipitates during continuous cooling [10,12,13], or by isothermal annealing at two different temperatures [11,14], has often been attributed to multiple distinct bursts of nucleation of precipitates at different undercoolings below the  $\gamma'$  solvus. These multiple nucleation bursts in turn result from the complex interplay of continuously increasing thermodynamic driving force for nucleation (chemical free energy difference) due to increasing undercooling, reduction in this driving force due to previous nucleation events and the rapidly declining diffusivity of alloying elements with decreasing temperature. At lower undercoolings (or higher temperatures, just below the  $\gamma'$  solvus temperature) lower driving force for nucleation coupled with higher diffusivities leads to the first burst of  $\gamma'$  nucleation forming the first generation of precipitates with low nucleation density, often referred to as primary  $\gamma'$  precipitates. At higher undercoolings, reduced diffusivity of atoms leads to supersaturation of  $\gamma'$ -forming elements away from the diffusion fields of the growing primary  $\gamma'$  precipitates, and coupled with a greater thermodynamic driving force results in further bursts of nucleation, consequently forming secondary (or tertiary in some cases)  $\gamma'$  precipitates with a high nucleation density [6,10,11]. This mechanism has been discussed in the phase field modeling studies by Wen et al. [10], where the Ginzburg–Landau equation has been coupled with the non-linear Cahn–Hilliard diffusion equation. In order to simulate the precipitation sequence during continuous cooling of the Ni–Al alloy, a Langevin stochastic term was introduced while accounting for the contribution due to undercooling. Their results show a bimodal distribution of  $\gamma'$  particles with a significant gap between the two nucleation events. The shut-off of nucleation at high temperatures could be attributed to the soft impingement (overlap of diffusion fields) of first-generation  $\gamma'$  precipitates. At lower temperatures (higher cooling) due to increased supersaturation of elements like Ti and Al, in between the  $\gamma'$ -free channels a

subsequent nucleation event may take place. Similar studies have been done by Radis et al. [12], where they employed classical nucleation theory involving long range diffusion of atoms to understand nucleation kinetics of both monomodal as well as multimodal size distributions of  $\gamma'$  precipitates in the commercial nickel base superalloy Udimet 720. A slightly different approach was adopted by Boussinot et al. [14], where phase field modeling was conducted to simulate isothermal annealing at two different temperatures, which led to nucleation of two different  $\gamma'$  generations. At a higher temperature the Ni–Al alloy was aged for a sufficiently long time period to permit equilibration of the far-field  $\gamma$  composition and volume fraction of  $\gamma$  and the first-generation  $\gamma'$  precipitates. Subsequently on quenching to a lower temperature a second generation of  $\gamma'$  precipitates are formed that are considerably smaller in size and larger in number density when compared to the first-generation precipitates. Further annealing at this temperature results in the growth of the smaller precipitates. However, not all precipitates grow continuously. The smaller particles that are situated near the larger precipitates start decreasing in size and eventually disappear at the expense of the growth and coarsening of the latter. This diffusion-mediated interaction of the two generations of  $\gamma'$  precipitates is strongly dependent on the volume fraction of the larger precipitates, which in turn governs the  $\gamma$  channel width within which subsequent precipitation may take place. A similar investigation was done by Wen et al. [11], where the growth kinetics and evolution of precipitate number density with time were obtained by conducting isothermal annealing studies at different temperatures.

Three-dimensional (3-D) characterization of the morphology, size distribution and composition of  $\gamma'$  precipitates in Ni base alloys has been previously attempted via atom probe tomography (APT) for finer scale  $\gamma'$  precipitates and serial sectioning in a dual-beam focused ion beam (FIB) for coarser scale  $\gamma'$  precipitates, and these studies have been extensively reviewed in recent articles in the published literature [8,15–17]. These studies have been primarily conducted during annealing after rapid quenching of the alloy from the high temperature single  $\gamma$  phase field. Therefore, typically these studies have focused on a monomodal size distribution of refined  $\gamma'$  precipitates within the disordered  $\gamma$  matrix [8]. In addition, such APT studies have also focused on the partitioning of the alloying additions between these two phases and the segregation of certain alloying additions to the  $\gamma\gamma'$  interface as well as to grain boundaries. Serial sectioning and sequential scanning electron microscopy (SEM) imaging, carried out using a dual-beam focused ion beam system, followed by 3-D reconstruction, have also been recently used to investigate the 3-D morphology and distribution of larger scale primary  $\gamma'$  precipitates [18].

The above isothermal annealing studies, although quite important in understanding the nucleation and growth behavior of  $\gamma'$  precipitates, are quite different from the typical industrially relevant heat treatments. In the latter case, the cooling rates employed after solutionizing/homogenizing

in the single  $\gamma$  phase field are substantially slower than water-quenching and therefore often lead to the formation of multiple size ranges of  $\gamma'$  precipitates. Therefore, the focus of the current paper is on determining the morphology, distribution and composition of multiple generations of  $\gamma'$  precipitates, of different size ranges, formed during continuous cooling of Rene 88 DT as well as the compositional partitioning between these  $\gamma'$  precipitates and the adjoining  $\gamma$  matrix. The elemental partitioning as well as the 3-D morphology of the finest scale of  $\gamma'$  precipitates have been primarily characterized by APT. While APT affords a nanometer-scale resolution of structure and chemistry, it offers limited information in terms of the sampled volume of reconstruction and consequently is not the method of choice for analyzing coarser  $\gamma'$  precipitates. Thus in order to better understand the overall representative morphological features over larger length scales, SEM and energy filtered transmission electron microscopy (EFTEM) have been found to be more suitable methods [13,19].

The four primary objectives of this paper are as follows:

1. to identify the different generations of  $\gamma'$  precipitates that form during continuous cooling of a nickel base superalloy via in situ high energy X-ray diffraction studies carried out in a synchrotron;
2. to analyze size distribution and morphology of multiple generations of  $\gamma'$  precipitates, formed during continuous cooling at a relatively slow rate from the solutionizing temperature (single  $\gamma$  phase-field) using SEM and EFTEM;
3. to carry out detailed compositional analysis of the different generations of  $\gamma'$  precipitates as well as their near- and far-field  $\gamma$  compositions using APT and to investigate the  $\gamma$ - $\gamma'$  compositional partitioning and associated diffusion fields and interface widths;
4. to develop a better physical understanding of the mechanism of  $\gamma'$  precipitation in these alloys as a function of undercooling (below the  $\gamma'$  solvus temperature).

## 2. Experimental procedure

The bulk chemical composition of the commercially procured Rene 88 DT alloy was 56.53 Ni–16.24 Cr–13.27 Co–3.92 Ti–2.09 Al–4.08 Mo–3.92 W–0.76 Nb (wt.%) or 55.63 Ni–18.02 Cr–13.00 Co–4.74 Ti–4.45 Al–2.48 Mo–1.21 W–0.46 Nb (at.%). Material was cut from the bore and rim section of a disk, produced and tested under work supported by the Defense Advanced Research Projects Agency, Defense Sciences Office (Engine Systems Prognosis, Contract Nos. HR0011-04-C-0001 and HR0011-04-C-0002). The program evaluated the impact of microstructure on mechanical properties [20]. The samples were supersolvus-solution-treated in a vacuum furnace at 1150 °C in the single  $\gamma$  phase field for 30 min to dissolve any existing  $\gamma'$  and then slow-cooled at an average cooling

rate of 24 °C min<sup>−1</sup> (to be subsequently referred to as SC0). These samples were subsequently aged for a period of 1 and 15 h, at 760 °C in a large chamber vacuum furnace and air quenched. In this paper these samples will be referred to as SC1 and SC15 respectively.

For synchrotron studies, high-energy X-ray diffraction (HEXRD) was performed at beamline 11-ID-C at the Advanced Photon Source (APS) facility in Argonne National Laboratory. A beam energy of 115 keV (equivalent to a wavelength of 0.1078 Å) and a beam size of 0.5 mm by 0.5 mm were used for the diffraction studies. Rene 88 DT samples, roughly 5 mm in diameter and 2 mm in thickness, were loaded in a Linkam TS1500<sup>TM</sup> furnace that was kept in an argon atmosphere. The diffraction patterns were collected at a time interval of 30 s with a Perkin-Elmer two-dimensional (2-D) detector located at a distance of 1.6 m from the sample.

Samples for APT studies were prepared by focused ion beam milling technique. For this purpose, samples were prepared by a dual-beam FIB instrument (FEI Nova Nanolab 200) system using a Ga ion beam. The ion beam thinning was carried out in multiple steps, starting with 30 kV ions and finally finishing with 5 kV ions to reduce the surface damage caused by the higher energy ions [21]. The final tip diameter of the atom probe specimens was ~50–80 nm. The APT experiments were carried out using a LEAP 3000 local electrode atom probe (LEAP<sup>TM</sup>) system from Cameca Inc. All atom probe experiments were carried out in the electric-field evaporation mode at a temperature of 70 K, with the evaporation rate varying from 0.2 to 1.0% and the pulsing voltage at 30% of the steady-state applied voltage.

TEM samples were also prepared via conventional routes, consisting of mechanical grinding and polishing of 3 mm diameter disks, followed by dimple grinding and finally ion-beam milling to electron transparency. Ion beam milling was conducted on a Gatan Duo Mill and Fischione Model 1010 ion milling system, operated at 6 kV. TEM analysis was conducted on a FEI Tecnai F20 field emission gun transmission electron microscope operating at 200 kV. Images were obtained using the Cr M-edge (42 eV) in the EFTEM mode, as described elsewhere [19]. Representative regions were imaged at different magnifications to capture the relevant secondary and/or tertiary  $\gamma'$  precipitates in the alloy.

SEM analysis of primary  $\gamma'$  precipitates were done using backscattered detector on etched samples. Prior to SEM analysis the samples were polished and etched using Keller's reagent (15 ml HCl + 10 ml glycerol + 5 ml HNO<sub>3</sub>).

## 3. Results

### 3.1. In situ X-ray diffraction studies of nucleation of multiple generations of $\gamma'$ precipitates

The  $\gamma'$  precipitation during slow continuous cooling of the Rene 88 DT alloy from above the  $\gamma'$  solvus temperature



at the rate of  $24\text{ }^{\circ}\text{C min}^{-1}$ , i.e. from the single  $\gamma$  phase field, has been investigated via in situ high energy X-ray diffraction studies, carried out using a high temperature furnace mounted on the synchrotron beam line at the Advanced Photon Source (APS) at the Argonne National Laboratory. The results of these diffraction studies are summarized in Fig. 1. Fig. 1a and b shows the progressive change in the intensity of the (001)  $\gamma'$  superlattice, and (111) fundamental reflections arising from both  $\gamma$  and  $\gamma'$  phases, as a function of temperature during in situ slow continuous cooling from the single  $\gamma$  phase field. Fig. 1a shows a sudden increase in (001) peak intensity during cooling between  $1284\text{ }^{\circ}\text{C}$  and  $1174\text{ }^{\circ}\text{C}$ , which then increases gradually with further reduction in temperature. The combined (111) reflection from  $\gamma'$  and  $\gamma$  phases shows a gradual increase in intensity during the same cooling cycle as shown in Fig. 1b. A simple first order approximation of the change in volume fraction of  $\gamma'$  as a function of temperature during continuous cooling can be qualitatively measured by plotting the ratio of the intensities of (001)  $\gamma'$  peak to (111)  $\gamma' + \gamma$  peak at every temperature, as shown in Fig. 1c. The plot clearly shows that during the cooling experiment, the intensity of the (001)  $\gamma'$  peak starts increas-

ing at a temperature marginally higher than  $1200\text{ }^{\circ}\text{C}$ , corresponding to the onset of the first nucleation burst. With decreasing temperature there is a continuous increase in the above intensity ratio, with a maximum at  $\sim 1000\text{ }^{\circ}\text{C}$ . On subsequent cooling, there is another increase in the intensity ratio with an onset at a temperature  $\sim 800\text{ }^{\circ}\text{C}$  with an actual maximum at  $\sim 700\text{ }^{\circ}\text{C}$  (Fig. 1c). These peaks observed in the (001)  $\gamma'$  peak to (111)  $\gamma' + \gamma$  peak intensity ratio give an indication of various  $\gamma'$  nucleation bursts, eventually resulting in a multimodal size distribution of  $\gamma'$  precipitates. It is important to note that the relative increase in this intensity ratio is directly proportional to the volume fraction of newly formed  $\gamma'$  precipitates and with decreasing temperature, the relative increase in  $\gamma'$  volume fraction with each successive generation decreases. This is clearly seen from Fig. 1c, where the increase in intensity, corresponding to the first nucleation burst, is significantly greater than that attributable to the second burst. Also, while only two distinct  $\gamma'$  nucleation bursts are visible in Fig. 1c, a possible third burst at much lower temperatures cannot be ruled out since it possibly leads to a rather small, and consequently difficult to detect, change in the intensity ratio. Fig. 1a and b also shows a systematic shift in the (001)  $\gamma'$  as well as (111)  $\gamma' + \gamma$  intensity peaks, indicating a decrease in lattice parameter for both  $\gamma'$  and  $\gamma$  phases with decreasing temperature. This decrease in lattice parameters can possibly be attributed to the combined effect of thermal contraction and the chemical partitioning between  $\gamma'$  and  $\gamma$  phases. However, the changes in lattice parameters are not equal for  $\gamma'$  and  $\gamma$  phases as seen in Fig. 1a and b, which gives rise to an increase in the  $\gamma'/\gamma$  lattice mismatch with decreasing temperature as reported previously for the Rene 88 DT alloy [22]. This also alludes to the fact that the ordered  $\gamma'$  phase is more stable with respect to temperature changes and therefore the change in lattice parameter with temperature is minimal for this phase.

### 3.2. Precipitate size and morphology

Slow cooling (SC0) of Rene 88 DT from a temperature exceeding the  $\gamma'$  solvus resulted in a multimodal distribution of precipitates as mentioned earlier. This multimodal distribution of precipitates can be divided into different groups based on their size, morphology and number density. These parameters in turn depend on the undercooling corresponding to the specific nucleation event, resulting in that particular population of precipitates. The different populations of  $\gamma'$  precipitates were characterized by coupling backscatter SEM studies with EFTEM studies.

Fig. 2a and b shows low and high magnification backscatter SEM images of the SC0 sample with  $\gamma'$  precipitates exhibiting a darker contrast. As seen from the figure, the larger first-generation  $\gamma'$  precipitates develop largely a cuboidal morphology or in some cases an irregular morphology, due to coarsening or impingement of neighboring  $\gamma'$  precipitates. Henceforth, these first-generation  $\gamma'$

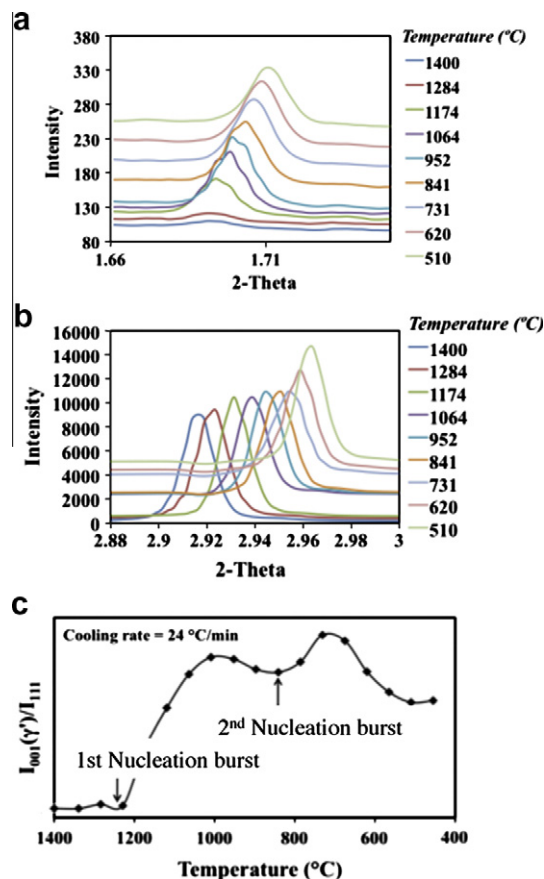


Fig. 1. Progressive change in the intensity of (a) (001)  $\gamma'$  superlattice, and (b) (111) fundamental reflections arising from both  $\gamma$  and  $\gamma'$  phases as a function of temperature during slow continuous cooling of Rene 88 DT alloy (SC0) from the single  $\gamma$  phase field. (c) A plot showing the ratio of (001)  $\gamma'$  to (111)  $\gamma' + \gamma$  peak intensities over a range of temperature.



precipitates will be referred to as primary  $\gamma'$  precipitates. These primary  $\gamma'$  precipitates have a relatively low number density, attributable to the smaller driving force for nucleation expected at lower undercooling. This is also evident on comparison with second and third generations of  $\gamma'$  precipitates forming at larger undercoolings (lower temperatures). Furthermore, there is a large variation in shape and size of the primary  $\gamma'$  precipitates. The size distribution of primary  $\gamma'$  precipitates is shown in Fig. 4a. The equivalent diameters of these  $\gamma'$  precipitates were determined by measuring their respective areas and equating these areas to areas of equivalent circles. Due to the irregular shape of these precipitates, this method really provides a qualitative rather than a quantitative distribution of precipitate sizes. As expected from the figure, there is a large variation in the sizes of these precipitates, ranging from 100 to 400 nm in diameter, with the maximum number of precipitates lying in the size range of 150–250 nm. Thus it is clear

that the primary  $\gamma'$  precipitates of this size range can be analyzed based on SEM investigations.

The second-generation, secondary  $\gamma'$  population that nucleates at lower temperatures due to a very high thermodynamic driving force grows at much lower rates due to the limited diffusivity at the lower temperatures. Imaging these rather small second-generation  $\gamma'$  precipitates is difficult using SEM, and therefore EFTEM imaging was employed, as shown in Fig. 3a and b. These EFTEM images are recorded using the Cr M-edge in the electron energy loss spectrum, obtained from the same sample. As observed in the images, the  $\gamma'$  precipitates exhibit a darker contrast being depleted in Cr [13,19]. As discussed earlier, the number density of the secondary  $\gamma'$  precipitates is clearly much larger than those of the primary  $\gamma'$  precipitates. This could be attributed to high nucleation rate at high undercoolings. Furthermore, as seen in the higher magnification EFTEM image in Fig. 3b, the primary  $\gamma'$  precipitates are separated from the secondary  $\gamma'$  precipitates by a precipitate-free depleted zone. Due to limited growth these secondary  $\gamma'$  precipitates exhibit near-spherical morphologies with size ranging from 12 to 30 nm in diameter. To clearly distinguish between the first and second generation of  $\gamma'$  precipitates, the size distribution for both precipitates have been also plotted in Fig. 4a. At this scale of analysis, a TEM imaging technique like EFTEM is the most suitable technique to measure the size of these precipitates and consequently find out their statistical size distribution.

On careful study of the higher magnification EFTEM image in Fig. 3b, a third population of extremely fine scale  $\gamma'$  precipitates is visible. These precipitates are present between the primary and secondary  $\gamma'$  precipitates, beyond the precipitate-free zone that surrounds the primary  $\gamma'$  precipitates. The extremely small size of these precipitates, even smaller than the secondary ones, may be a result of a third burst of nucleation at much lower temperatures (even higher undercooling). Due to their very small size and the limitations of EFTEM imaging in terms of spatial resolution, it is very difficult to accurately measure the size distribution of these precipitates using this technique.

### 3.3. Overall size distribution

The overall size distribution of different generations of  $\gamma'$  is shown in Fig. 4a and b. As seen in this figure, both bursts of nucleation give rise to two distinctly different populations of  $\gamma'$  with each nucleation event probably occurring over a range of temperatures, starting with a high driving force for nucleation which gradually decreases. Both generations of  $\gamma'$  show similar distributions and have been fitted to classical Gaussian distributions in Fig. 4b. The average diameter of the primary  $\gamma'$  precipitates is  $\sim 191$  nm with a standard deviation of  $\sim 78$  nm, which is close to the fitted peak of the Gaussian at 188 nm. Secondary  $\gamma'$  precipitates have an average diameter of  $\sim 8$  nm and a standard deviation of  $\sim 7$  nm, which is also close to the peak of the Gaussian at  $\sim 9$  nm in Fig. 4b. Therefore for both the

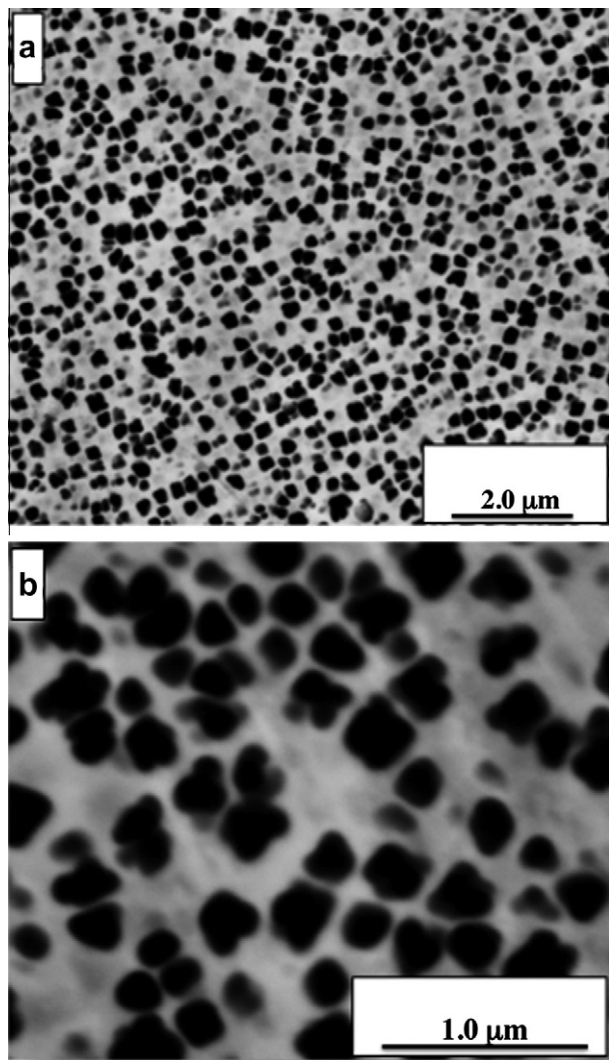


Fig. 2. (a) Low-magnification and (b) high-magnification backscatter SEM images of the SC0 sample with primary  $\gamma'$  precipitates exhibiting a darker contrast.

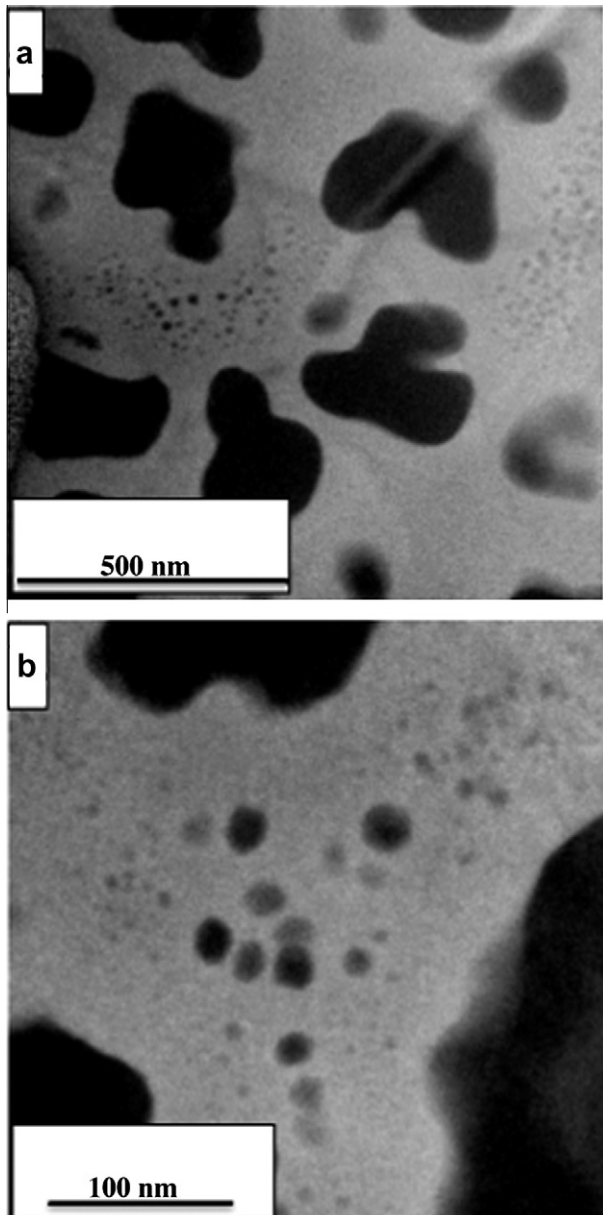


Fig. 3. (a) Low-magnification and (b) high-magnification energy-filtered transmission electron microscopy images obtained using Cr M-edge in the electron energy-loss spectroscopy spectrum of the SC0 sample. Along with primary  $\gamma'$  precipitates, the smaller secondary (and tertiary)  $\gamma'$  precipitates, which are Cr-depleted, exhibit darker grey contrast in these images.

first- and second-generation  $\gamma'$  precipitates, which were measured independently using SEM and EFTEM techniques respectively, the Gaussians are in close agreement with the actual frequency distributions. The salient points regarding the size distribution of  $\gamma'$  precipitates can be summarized as follows:

1. The size distribution of the primary  $\gamma'$  precipitates is quite large, ranging from  $\sim 100$  nm to  $\sim 400$  nm with a mean  $\sim 191$  nm, indicating that the nucleation of these precipitates takes place over a wide range of temperatures during continuous cooling.

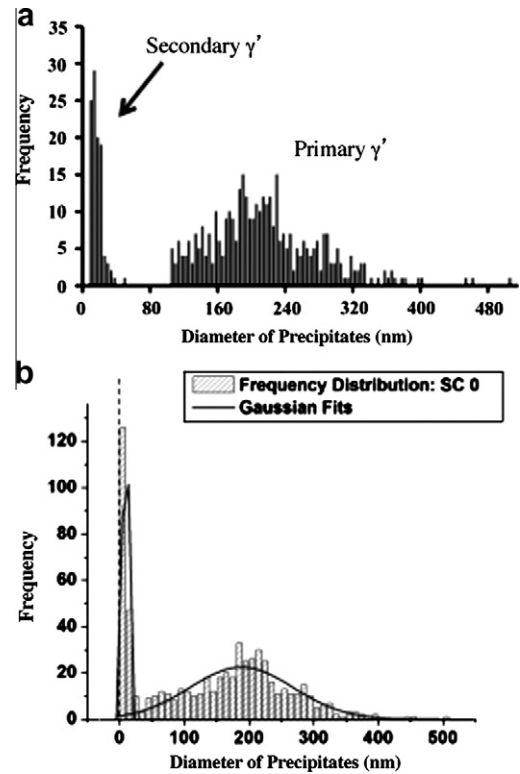


Fig. 4. (a) Precipitate size distribution plot of SC0 sample showing the size difference between the primary  $\gamma'$  and smaller secondary (and tertiary)  $\gamma'$  precipitates. (b) A Gaussian distribution used to fit the curves in (a) in order to determine the average diameter and standard deviation of different generations of precipitates.

2. Second-generation, secondary  $\gamma'$  precipitates have a much higher number density as compared to primary  $\gamma'$  precipitates.
3. The distributions observed in this study also indicate that each nucleation burst occurs over a range of temperatures.
4. Within each temperature window for a specific generation of  $\gamma'$  precipitates, the larger number of precipitates nucleates at lower temperatures and a smaller number nucleates at higher temperatures.

As mentioned earlier, a third generation of (tertiary)  $\gamma'$  precipitates is also present in this SC0 sample. However, the size distribution of the tertiary population cannot be accurately quantified using EFTEM. Thus only an average size of these precipitates could be determined and has been indicated by a dashed line in Fig. 4b. In order to identify and characterize this third generation of  $\gamma'$  precipitates, isothermal studies were conducted on the SC0 sample. The results of these studies are discussed later in this paper. The distribution also shows that the size difference between primary and secondary  $\gamma'$  is more as compared to secondary and tertiary  $\gamma'$  populations. This can be attributed to the higher diffusivity at high temperatures (where the primary precipitates form), leading to their more rapid growth while the growth of the secondary and tertiary precipitates

is rather limited at their lower formation temperatures. While previously reported modeling studies, based on classical nucleation theory, predict the formation of these multiple generations of  $\gamma'$  precipitates and their size distributions [10–12] this study is one of the first reports presenting direct experimental evidence of the size distribution associated with different generations of  $\gamma'$  precipitates forming during continuous cooling of a nickel base superalloy.

### 3.4. Compositional analysis of different generations of $\gamma'$

The compositional analysis of different generations of  $\gamma'$  precipitates has been carried out using atom probe tomography (APT). Fig. 5a shows a 3-D atom probe reconstruction of the SC0 sample. For simplicity, only two atomic species, Al and Cr, have been shown in the figure. The red ions represent Al ions whereas blue represent Cr ions.

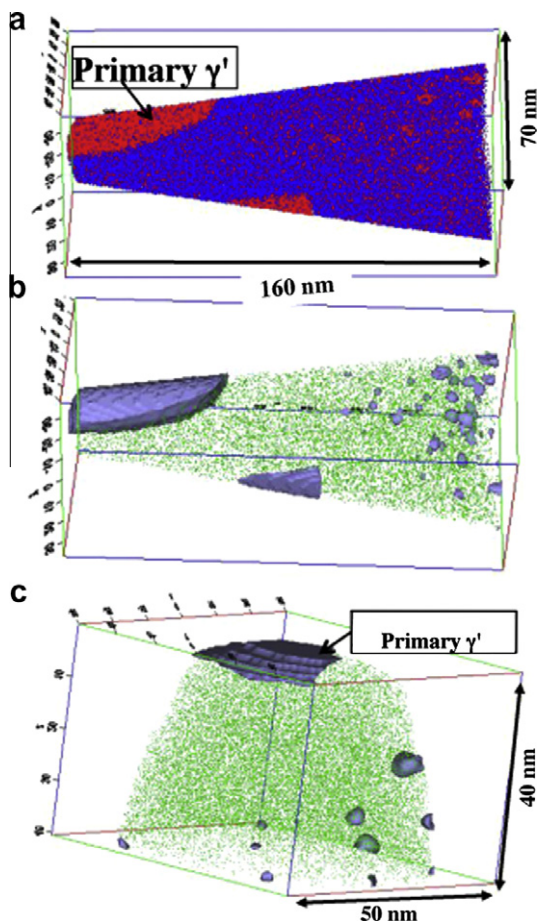


Fig. 5. (a) APT reconstruction of Cr (blue) and Al (red) atoms in a slow cooled (SC0) sample. The  $\gamma'$  precipitates are the Al-rich red regions with Cr-rich blue  $\gamma$  matrix. (b) An isosurface of the above reconstruction using 14 at.% Cr superimposed on Ni ions, where the  $\gamma'$  precipitates have a leaner amount of Cr. The different generations of  $\gamma'$  precipitates are clearly visible. (c) A second example in terms of atom probe reconstruction (Cr = 14 at.% isosurface along with Ni ions) of the same SC0 sample. (For interpretation of the references to colour in this figure legend, the reader is referred to the web version of this article.)

This reconstruction clearly shows that the Al and Cr partition to the  $\gamma'$  and  $\gamma$  phases respectively. A better visual representation of the same 3-D reconstruction is shown in Fig. 5b, where an iso-concentration surface (or isosurface in short) using 14 at.% Cr has been plotted along with the Ni ions (in green). This isosurface view clearly shows sections of two large primary (first generation)  $\gamma'$  precipitates along with multiple fine scale  $\gamma'$  precipitates. Going by the size of these fine scale particles, they are either tertiary or secondary precipitates at the smaller end of their size distribution. These precipitates are also clearly visible from the EFTEM image in Fig. 3b. A precipitate-free  $\gamma'$  depletion zone, containing only Ni ions, between the two different sizes of precipitates is also observed from the reconstructions in Fig. 5. A second atom probe reconstruction (Cr = 14 at.% isosurface along with Ni ions) of the same SC0 sample is shown in Fig. 5c. This figure also shows a section of a primary  $\gamma'$  precipitate, multiple tertiary (or secondary)  $\gamma'$  precipitates, and the precipitate-free zone in between.

The partitioning of the primary alloying elements in Rene 88 DT alloy, i.e. Al, Ti, Cr, Co and Mo, for two different generations of  $\gamma'$  precipitates, is shown in the compositional profiles in Fig. 6a and b respectively. These compositional profiles, represented in the form of proximity histograms (or proxigrams corresponding to a Cr = 14% isosurface) [23], clearly revealed that all the  $\gamma'$  precipitates, represented by the left side of the plot in each case, are enriched in Al and Ti and depleted in Cr, Co and Mo. However, from the steady state value on the left of the proxigrams, it can be said that the relative compositions of primary and tertiary (or secondary) precipitates is substantially different. Thus the primary  $\gamma'$  precipitates contain a higher amount of Al and Ti, whereas the tertiary  $\gamma'$  have lower Al and Ti and higher Co and Cr, as evident after comparing Fig. 6a and b respectively. Even though there is a variation in size of the smaller  $\gamma'$  precipitates, the variability in composition between different precipitates was observed to be minimal. This indicates that even though the tertiary (or secondary) precipitates form over a range of temperatures, large variations in composition within this particular generation do not occur. Fig. 6c compares the Al and Cr compositional profiles across the  $\gamma'/\gamma$  interface for a specific large (primary) and a small (tertiary or secondary)  $\gamma'$  precipitate. This comparison clearly reveals the substantially more diffuse interface in the case of the smaller precipitates (plotted using dotted lines) as compared with the primary ones (plotted using bold lines). Similar evidence of a larger compositional width of the  $\gamma'/\gamma$  interface in the case of smaller tertiary (or secondary) precipitates, indicating a compositionally diffuse interface, was observed in the case of many other precipitates analyzed in the same manner. It should also be noted that in addition to the tertiary  $\gamma'$  precipitates clearly delineated from the  $\gamma$  matrix using the Cr–14 at.% isosurface construction, the raw ionic reconstruction, shown in Fig. 5a, also reveals pockets of local enrichment of Al ions (in red) between tertiary  $\gamma'$



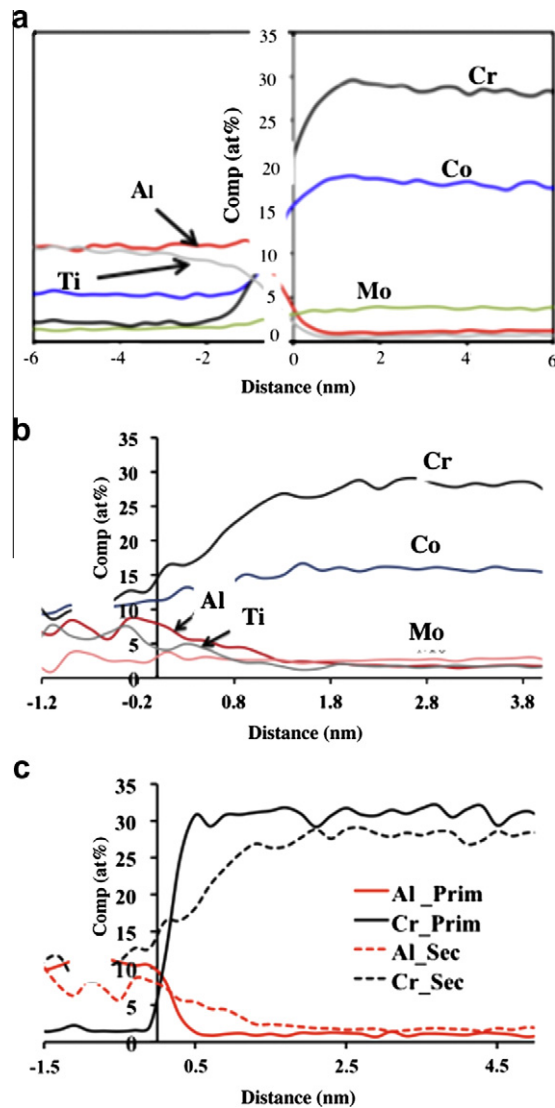


Fig. 6. Proximity histograms of (a) primary  $\gamma'$  and (b) secondary (or tertiary)  $\gamma'$  precipitates in SC0 sample using a Cr = 14 at.% isosurface. The plots show the partitioning of the primary alloying elements, i.e. Al, Ti, Cr, Co and Mo, between the  $\gamma$  and  $\gamma'$  phases. (c) Plot comparing the Al and Cr compositional profiles across the  $\gamma/\gamma'$  interface for two specific large (primary) and small (tertiary or secondary)  $\gamma'$  precipitates.

and the depletion zone. These small pockets are possibly far from equilibrium in composition but still depleted in Cr and enriched in Al as compared to the  $\gamma$  matrix, and could potentially act as the nucleation sites for  $\gamma'$ .

While each generation of  $\gamma'$  has a different composition, the  $\gamma$  region near these  $\gamma'$  precipitates also exhibits local compositional variations. Fig. 7a shows a proxigram that is plotted across a primary  $\gamma'$  precipitate, on the left, to a precipitate-free  $\gamma'$  depletion zone towards the right. The plot shows the near-field and far-field compositions of the  $\gamma$  matrix. Right next to the primary  $\gamma'$  precipitate the  $\gamma$  matrix shows a near-equilibrium composition. From the plot it is evident that primary  $\gamma'$  precipitate (represented by the region on the left) contains higher amounts of Al and Ti whereas the depletion zone is enriched in Cr and

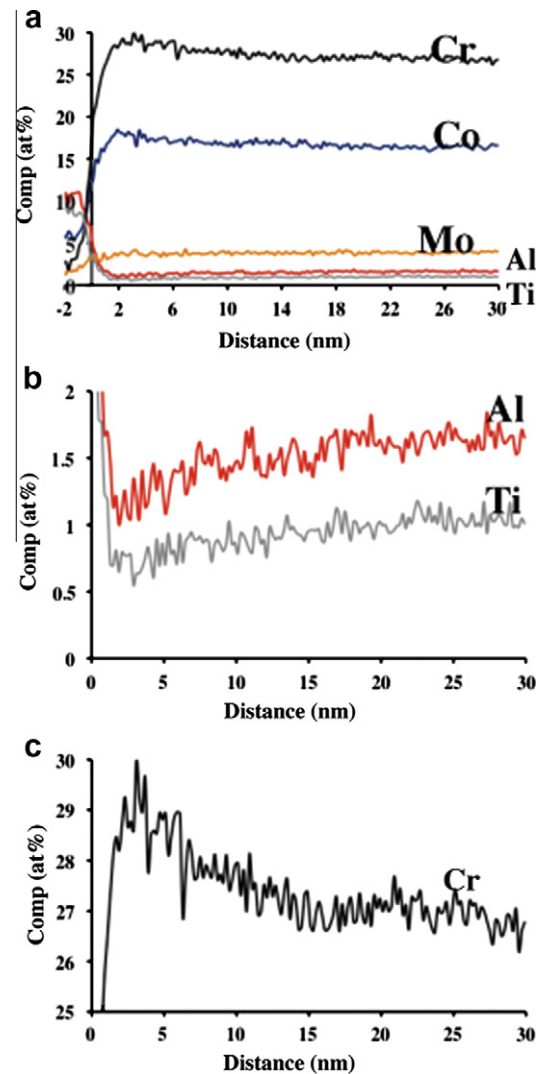


Fig. 7. (a) Proximity histograms of the SC0 sample plotted from a primary  $\gamma'$  precipitate on the left to a precipitate-free  $\gamma'$  depletion zone towards the right. The plot shows the near-field and far-field compositions of the  $\gamma$  matrix. Magnified images of the above proximity histogram showing the compositional variation of (b) Al and Ti and (b) Cr near and far away from the primary  $\gamma'$  precipitate.

Co. The compositional gradient across the interface also appears sharp. Mo partitioning across the interface is not large even though it seems to be partitioning more towards the  $\gamma$  matrix. From left to right, the proxigram shows a slight decrease in the Cr and Co content, suggesting a change in composition within the precipitate-free  $\gamma$  matrix. Thus as one probes away from the primary  $\gamma'$  precipitate, the  $\gamma$  composition within the depletion zone also departs further away from equilibrium. This variation in composition within the  $\gamma$  matrix, near and away from the primary  $\gamma'$  precipitate, is also observed in the case of Al and Ti, as evident from the magnified view of the proxigram (Fig. 7b). It can be clearly seen that right next to the  $\gamma/\gamma'$  interface there is a local depletion of Al and Ti ( $\sim 1.7$  at.% and  $0.5$  at.% respectively) which gradually increases ( $\sim 1.7$  at.% and  $1$  at.% respectively) as one probes away from the primary

$\gamma'$  precipitate. Similar to Fig. 7b, Fig. 7c shows a magnified view of the Cr composition profile across the  $\gamma'/\gamma$  interface. The trend followed by this plot is an inverse of the plots shown in Fig. 7b. Thus, there is a local enrichment of Cr next to the interface ( $\sim 30$  at.%) which slowly decays to  $\sim 27$  at.% inside the depletion zone. These observations show that in Rene 88 DT alloy there exists a compositional gradient within the precipitate-free region of the  $\gamma$  matrix, where the composition of all the major alloying additions slowly changes from near-equilibrium to far-from-equilibrium as one moves away from the interface into the  $\gamma$  matrix. However, as expected this gradient is much more diffuse in comparison to the compositional gradient observed across the  $\gamma'/\gamma$  interface. Additionally, it should be noted that the far-field composition of this precipitate-free region within the  $\gamma$  matrix is enriched in Cr and Co, and depleted in Al and Ti, as compared to average alloy composition.

From Fig. 6 it is clear that the compositions of coarser and finer  $\gamma'$  precipitates are close to equilibrium, and far from equilibrium, respectively. However, a closer examination of the atom probe reconstruction in Fig. 5a showing the  $\gamma$  region near the depletion zone reveals some interesting details. Fig. 8a and b shows 2-D compositional maps of Cr, created using a 2 nm thick region of interest (RoI) across primary and tertiary (or secondary)  $\gamma'$  precipitates, along with the depleted zone lying in between. These maps are pseudo-colored based on the composition, with color changes from blue to yellow to red, representing progressively increasing Cr content. While Fig. 8a shows the map with an overlapping 14 at.% Cr isosurface, Fig. 8b shows only the 2-D compositional map. Comparing the two figures, the primary  $\gamma'$  precipitate in the bottom left corner (Fig. 8a) is substantially depleted in Cr and thus is blue in color (Fig. 8b). However, around this primary precipitate, near the  $\gamma'/\gamma$  interface, a yellow colored interfacial layer is observed which is in between the blue and red contrast. This suggests a progressive decrease in Cr content from the  $\gamma'$  precipitate to the  $\gamma$  matrix. Again the smaller precipitates in the top right of Fig. 8a have intermediate Cr contents (refer to Fig. 6b) and are thus yellow in color. Apart from this, Fig. 8b also shows nanometer-scale pockets within the depleted region that are locally depleted in Cr, as they exhibit a light yellow contrast. However the corresponding Cr isosurface in Fig. 8a does not delineate these regions. This indicates that these nanoscale regions have not yet reached the composition of 14 at.% Cr. These regions are non-spherical in morphology and from the isosurface generated using 18 at.% Cr, shown in Fig. 8c, it is clear that the Cr-rich and Cr-lean regions are interconnected in nature within the  $\gamma'$  depleted region as well as in the regions where the fine scale tertiary (or secondary) precipitates are formed. Thus in this figure all the regions containing less than 18 at.% Cr are shown in blue, while the regions in between contain more than 18 at.% Cr. The interconnected nature of these compositionally phase separated regions is a possible indication of a spinodally

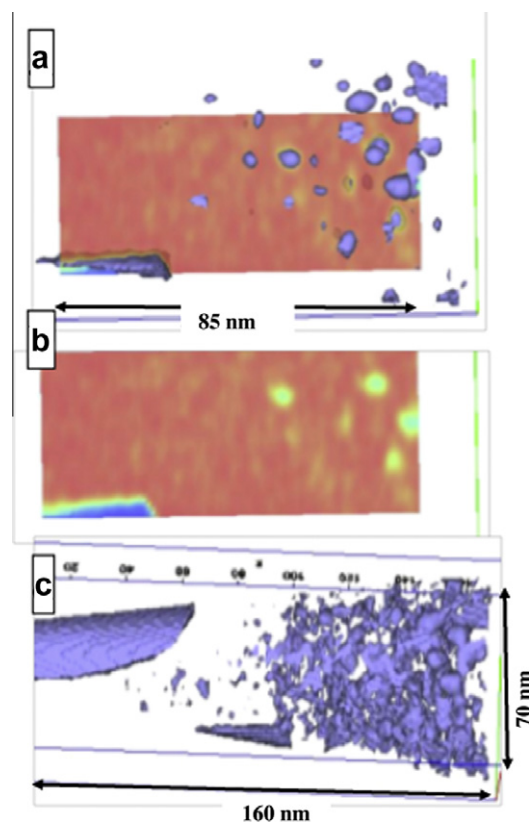


Fig. 8. A 2-D compositional map of Cr, created using a 2 nm thick region of interest across primary and tertiary (or secondary)  $\gamma'$  precipitates, along with the depleted zone lying in between them, (a) with and (b) without an overlapping isosurface that was generated using 14 at.% Cr (showing regions that are equal to or less than 14 at.% Cr). (c) An isosurface of the above reconstruction using 18 at.% Cr, showing the interconnected nature of Cr-rich and Cr-lean regions.

decomposed matrix exhibiting a continuous variation in composition, rather than discrete pockets that reach an equilibrium composition via a classical nucleation and growth process [24]. It needs to be reiterated that the regions that exhibit this continuous network of Cr-depleted pockets are farthest away from the equilibrium  $\gamma$  composition, and presumably form at the highest undercooling. Thus, as expected, these interconnected regions are not present near the precipitate-free depletion zone, which seems to be closer to the equilibrium composition of the  $\gamma$  matrix.

This proposition can be further strengthened using the composition profiles that were discussed in Fig. 6. Comparing the proxigrams generated from primary and secondary (or tertiary) precipitates it is evident that the former exhibits a compositionally sharper interface when compared to the latter. This is in accordance with the prediction of Cahn and Hilliard [24], who mentioned that at lower supersaturations (lower undercooling) the nucleus exhibits more classical-like behavior with a near-equilibrium composition and the region around this classical nucleus also approaches an equilibrium composition. However, as supersaturation increases, corresponding to larger undercoolings (or lower precipitation temperatures) encountered

by the smaller scale secondary or tertiary  $\gamma'$  precipitates, the nucleus starts losing its resemblance to a classical nucleus. Thus at higher undercooling, both Helmholtz free energy as well as gradient energy factors contribute to the diffuseness of the interface. Also no part of this non-classical nucleus is approximately homogeneous and the composition at its center is substantially lower than that of a classical nucleus. Another similar non-classical decomposition pathway that has been discussed in the literature, and also applicable to  $\gamma'$  precipitation within the disordered  $\gamma$  matrix, is phase separation (or composition clustering) via spinodal decomposition followed by ordering within the appropriate phase separated pockets [25–28]. Such decomposition is expected to take place in systems that have been undercooled to a large extent below the equilibrium transformation temperature. When a disordered solid solution is rapidly cooled (or quenched) from a single-phase field to a temperature corresponding to a two-phase field, the resulting highly undercooled and supersaturated disordered solid solution is often unstable (or metastable) with respect to both clustering and ordering processes [25]. Experimental evidence of such a decomposition pathway in nickel base alloys has been previously reported in the literature in the case of binary Ni–Al [26] and Ni–Ti alloys [27], as well as in a recent study on very fast quenched Rene 88 DT [28]. The important difference to note is that while in these systems that have been rapidly cooled to low temperatures below the equilibrium transformation temperature, a monomodal size distribution of ordered  $\gamma'$  precipitates result, in the present study there are multiple generations of  $\gamma'$  precipitates and the mechanism of spinodal decomposition followed by ordering might be applicable to only the second (or third) generation of precipitates. However, more detailed investigations are required in order to develop a more detailed understanding of the precipitation mechanism applicable to the refined second or third generation of ordered precipitates.

### 3.5. Growth influenced morphology and chemical changes

Fig. 9a shows a 3-D atom probe reconstruction of the slow cooled and 760 °C/1 h aged (SC1) sample. The 160 nm × 100 nm × 100 nm reconstruction, generated using a Cr isosurface (blue) superimposed on Ni ions (green), clearly shows primary as well as smaller tertiary  $\gamma'$  precipitates. Similar to the SC0 condition shown in Fig. 5, the depletion zone between precipitates of two different generations is clearly visible in this reconstruction. The overall size of these precipitates was determined using the IVAS<sup>TM</sup> software and their equivalent diameters have been plotted in Fig. 9b. Similar to the studies conducted in the case of the SC0 sample, the first and second generation of primary and secondary  $\gamma'$  precipitates were imaged using SEM and EFTEM respectively (not shown), and subsequently their size distributions were measured. The compilation of this data, containing the equivalent diameters of three different  $\gamma'$  generations, obtained using three different

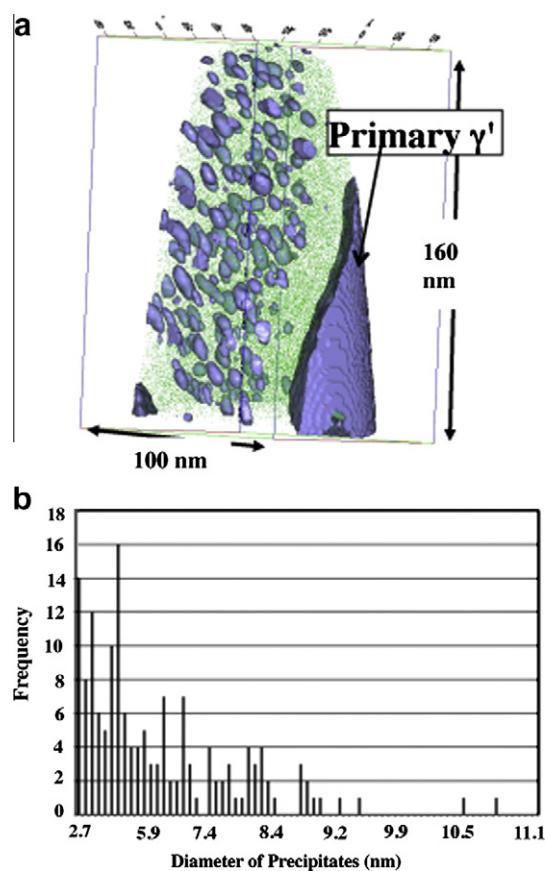


Fig. 9. (a) APT reconstruction of Cr (blue) and Al (red) atoms in the slow-cooled and 1 h aged (SC1) sample. The  $\gamma'$  precipitates are the Al-rich red regions with Cr-rich blue  $\gamma$  matrix. (b) Precipitate size distribution plot of the tertiary  $\gamma'$  precipitates generated using the IVAS<sup>TM</sup> software. (For interpretation of the references to colour in this figure legend, the reader is referred to the web version of this article.)

characterization tools, is shown in Fig. 10a. Unlike in SC0 condition (Fig. 4), this size distribution plot clearly shows three distinct populations (or size scales) of  $\gamma'$  precipitates, suggesting three distinct nucleation bursts corresponding to different undercooling values below the  $\gamma'$  solvus temperature. Fig. 10b shows a proximity histogram generated using the Cr isosurface that shows the variation of primary alloying elements in Rene 88 DT after aging for 1 h at 760 °C (SC1). Similar to the SC0 condition (Fig. 7), on moving away from the  $\gamma'/\gamma$  interface, while the near-field  $\gamma$  composition has reached equilibrium, the far-field  $\gamma$  composition is far from equilibrium and contains lower than equilibrium amounts of Cr and Co, and supersaturation of Al and Ti. Incidentally, comparing Figs. 9a and 10b, the  $\gamma$  compositions that were probed 20 nm beyond the  $\gamma'/\gamma$  interface in both cases were in the vicinity of tertiary  $\gamma'$  precipitates.

Similar studies were conducted on Rene 88 DT samples that were aged for 15 h. Fig. 11a shows an EFTEM image of the alloy that was aged for 15 h at 760 °C after solutionizing and slow cooling to room temperature (SC15). From Fig. 11a as well as the higher magnification image in



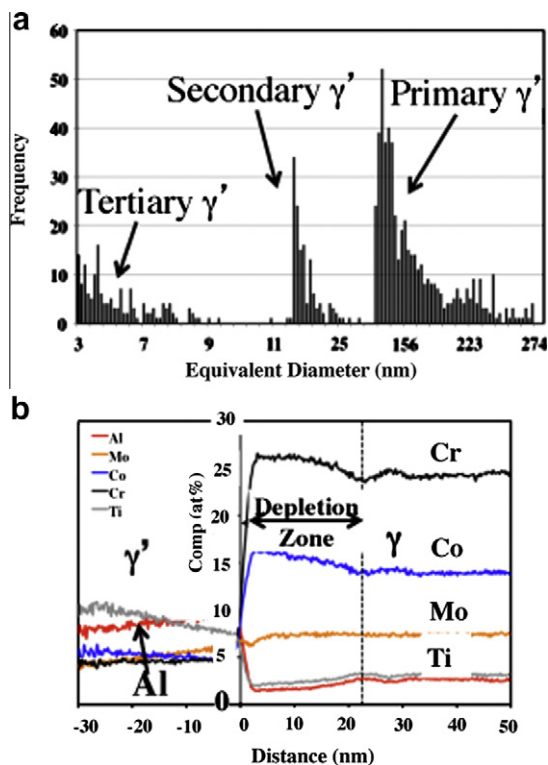


Fig. 10. (a) Precipitate size distribution plot of SC1 sample showing the size difference between the primary  $\gamma'$ , secondary  $\gamma'$  and tertiary  $\gamma'$  precipitates. (b) Proximity histograms of the SC1 sample plotted from a primary  $\gamma'$  precipitate on the left to the  $\gamma$  matrix towards the right. The plot shows the near-field and far-field compositions of the  $\gamma$  matrix.

Fig. 11b, it is clear that the smaller  $\gamma'$  precipitates are coarser than those in the SC0 condition. However, very limited changes are observed in the size of primary  $\gamma'$  precipitates or the depleted zone around them. Atom probe tomography was conducted with the SC15 sample so as to obtain the true morphology and size of the tertiary (or secondary)  $\gamma'$  precipitates and are shown in Fig. 12. As seen from the isosurfaces, generated using 14 at.% Cr (blue), superimposed on Ni atoms (green) (Fig. 12 a), the  $\gamma'$  precipitates have grown and are  $\sim 20$  nm in diameter after 15 h of aging. Also the size of the  $\gamma'$  precipitates closest to the primary precipitate appear to be smaller than the precipitates present at further distances from the primary precipitate, indicating the development of three distinct populations – primary, secondary and tertiary. The long-range composition profiles for the alloying elements across the primary  $\gamma'/\gamma$  interface into the precipitate-free depleted zone have been plotted by averaging across a cylindrical RoI as shown in Fig. 12b. These profiles clearly show that for all alloying elements the compositional profile within the precipitate-free depleted zone remains constant, clearly indicating that the far-field  $\gamma$  matrix has reached its equilibrium composition in this case. Consequently, there is no supersaturation of Al and Ti (or undersaturation of Cr and Co) present within the matrix that can lead to nucleation or growth of additional  $\gamma'$  precipitates.

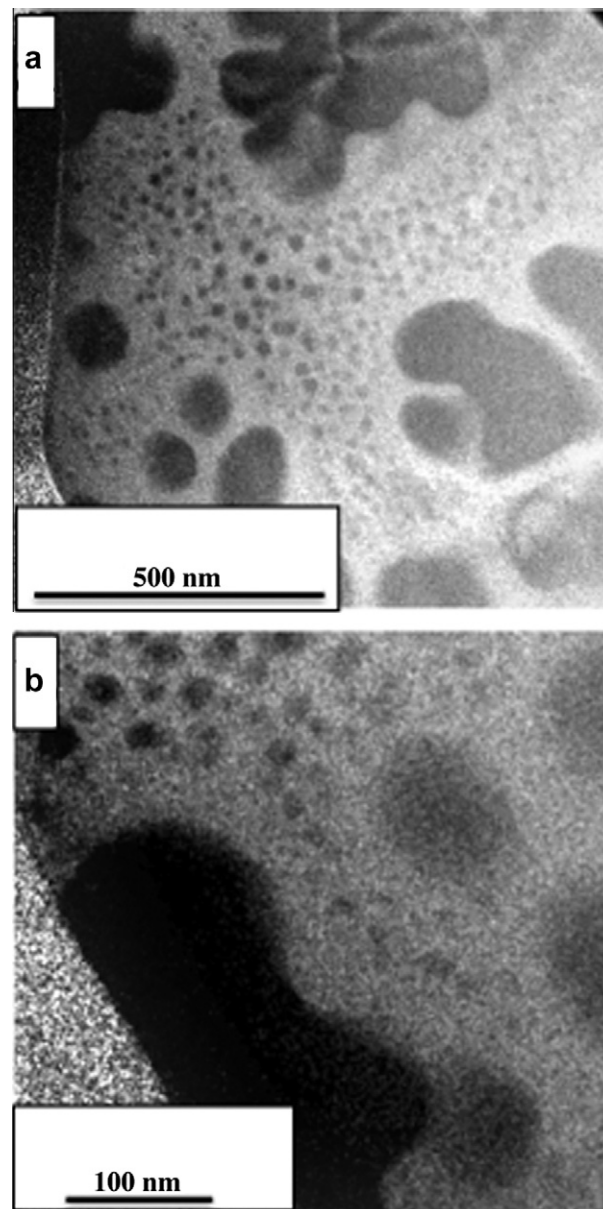


Fig. 11. (a) Low-magnification and (b) high-magnification energy-filtered transmission electron microscopy images obtained using Cr M-edge in the electron energy-loss spectroscopy spectrum of the SC15 sample. Along with primary  $\gamma'$  precipitates the smaller secondary (and tertiary)  $\gamma'$  precipitates which are Cr-depleted, exhibit the darker grey contrast in these images.

## 4. Discussion

### 4.1. Mechanism of multiple bursts of nucleation

Based on the detailed experimental results presented in this paper it is now possible to develop a mechanistic model leading to the multiple nucleation bursts of  $\gamma'$  precipitates during continuous cooling of a nickel base superalloy. This mechanism has been schematically shown using two representative figures, Figs. 13 and 14. During cooling, due to the continuous decrease in temperature below the  $\gamma'$  solvus,

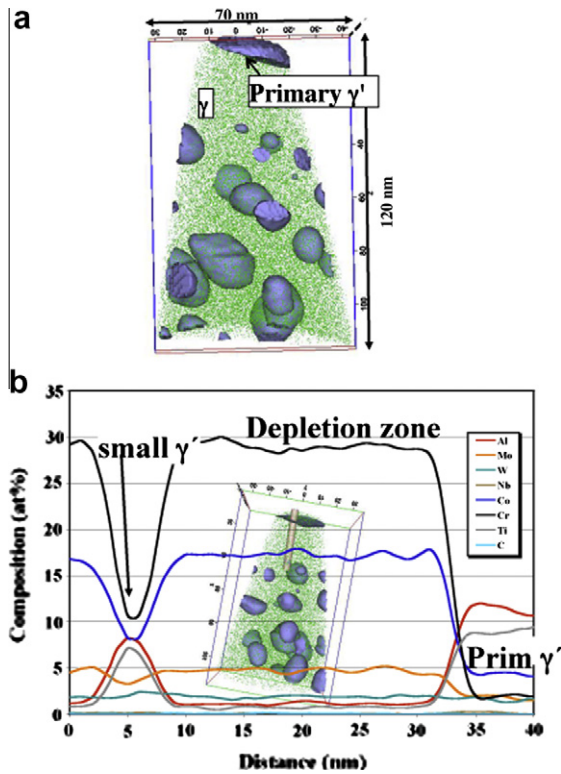


Fig. 12. (a) APT reconstruction of an isoconcentration surface, generated using 14 at.% Cr (blue) superimposed on Ni atoms (green), in slow-cooled and aged (SC15) sample. (b) A compositional profile, from a small tertiary (or secondary) to a large primary  $\gamma'$  precipitate with the depletion zone lying in between them, showing the variation of major alloying additions in SC15 sample. (For interpretation of the references to colour in this figure legend, the reader is referred to the web version of this article.)

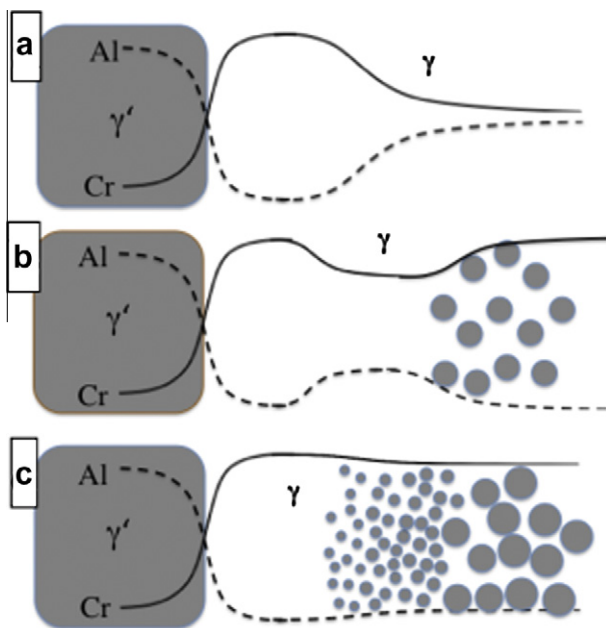


Fig. 13. (a–c) Schematic illustrations of how multiple  $\gamma'$  generations can form during slow cooling of Rene 88 DT alloy.

there is an increase in the thermodynamic driving force for nucleation associated with continuously increasing und-

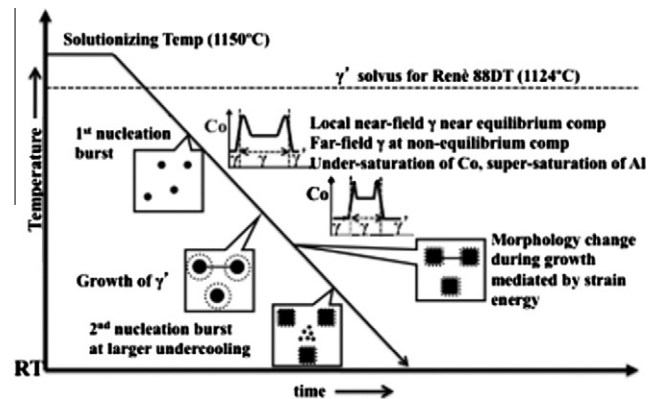


Fig. 14. Schematic illustrating the effect of cooling rate on the formation of different  $\gamma'$  generations in Rene 88 DT alloy.

ercooling. However as soon as the first generation of  $\gamma'$  precipitates is nucleated, this driving force is partially consumed, especially in the local region surrounding the first-generation (or primary) precipitates. Thus, the local region surrounding these primary  $\gamma'$  precipitates, also referred to as the near-field  $\gamma$  composition, is depleted in  $\gamma'$  forming elements, Al and Ti, and enriched in  $\gamma$  stabilizing elements, Co and Cr. Since the first nucleation burst occurs at relatively high temperatures (low undercooling below the  $\gamma'$  solvus), the higher diffusivity of the various alloying elements promotes their rapid partitioning between the  $\gamma'$  precipitate and the adjacent  $\gamma$  matrix. Also at these high temperatures, the primary  $\gamma'$  precipitates grow quite rapidly and develop a cuboidal to irregular morphology (Figs. 2 and 3 and schematic in Fig. 14) as anisotropic elastic strain energy starts dominating over the isotropic interfacial energy. However as temperature decreases, due to the reduced mobility of the solute elements, their redistribution becomes more and more difficult. Thus a condition similar to the schematic diagram in Fig. 13a occurs where the near-field  $\gamma$  composition, close to the primary  $\gamma'$  precipitates, reaches equilibrium (as suggested by a decrease in Al and increase in Cr). However as one probes away from the precipitate, far-field into the  $\gamma$  matrix, there is an enrichment of Al (and Ti) and depletion of Cr (and Co), primarily because of the inability of these regions to equilibrate rapidly at low temperatures (Fig. 13a). A schematic of a typical near-field near-equilibrium and far-field non-equilibrium composition profile for Co is shown in Fig. 14. This results in the formation of far-field supersaturated corridors within the  $\gamma$  matrix, which act as potential sites for  $\gamma'$  nucleation at lower temperatures when the relative driving force increases. Thus, at these lower temperatures, the higher thermodynamic driving force and higher nucleation rate result in a second nucleation burst, leading to a large number density of  $\gamma'$  precipitates, increasing the  $\gamma'$  volume fraction (corresponding to the increase in (001)  $\gamma'$  to (111)  $\gamma' + \gamma$  peak intensity ratio in Fig. 1). On further cooling these particles try to grow but their growth is severely restricted due to the low diffusivities. Thus the

second generation of precipitates has a higher number density and is smaller than the first generation of precipitates (Fig. 4 and schematic in Fig. 14). Furthermore, this high number density of secondary precipitates leads to small inter-precipitate distances and consequently results in rapid overlap of the diffusion fields (soft impingement), restricting their further growth. These precipitates are small enough such that the isotropic interfacial energy dominates over anisotropic elastic strain energy. This, coupled with the inherently low  $\gamma - \gamma'$  misfit in the case of Rene 88 DT, results in these secondary precipitates maintaining a near spherical morphology (Figs. 3 and 5). Also as discussed earlier, these secondary precipitates do not exhibit features of a classically nucleated precipitate of equilibrium composition, but rather exhibit both compositional inhomogeneities within them as well as relatively diffuse  $\gamma'/\gamma$  interfaces (Fig. 6). Changes also take place in the  $\gamma$  matrix that surround these precipitates. Thus the matrix becomes depleted in Al (and Ti) and enriched in Cr (and Co), as shown in the schematic diagram in Fig. 13b. Thus at this temperature the region close to the secondary  $\gamma'$  precipitates have a very low driving force for further nucleation. However Fig. 13b also shows that the  $\gamma$  matrix between the secondary  $\gamma'$  and the depleted zone (around the primary  $\gamma'$ ) still retains a non-equilibrium composition, involving, for example, an Al supersaturation (or Cr undersaturation). However, the thermodynamic driving force is not sufficient to cause any fresh nucleation until a really large undercooling is achieved. This undercooling occurs when the sample is cooled to further lower temperatures that leads to a third burst of nucleation, resulting in the population of tertiary  $\gamma'$  precipitates (schematic diagram in Fig. 13c). However, slower kinetics and limited supersaturation of solute at this stage further limit the growth of these tertiary  $\gamma'$  precipitates. Thus a large number of fine scale spherical  $\gamma'$  precipitates are formed. It should be noted that typically the tertiary  $\gamma'$  precipitates are nucleated in between the primary and secondary  $\gamma'$  precipitates but closer to the secondary precipitates, primarily because the depletion zone around a secondary  $\gamma'$  precipitate is much smaller than that of primary  $\gamma'$  precipitate (Fig. 13c). Summarizing, several thermodynamic and kinetic factors such as driving force for nucleation, number density of nucleation sites (related to the nucleation rate) and diffusivity determine the formation of multiple generations of  $\gamma'$  precipitates and the complex interplay of these factors gives rise to the multiscale microstructures that are experimentally observed on continuous cooling. These observations are in excellent agreement with the phase field simulations reported previously [10] as well as with experimental investigations in some commercial nickel base superalloys [6,9,12], where continuous cooling results in shrinkage of diffusion fields associated with larger  $\gamma'$  precipitates, consequently opening up precipitate-free supersaturated  $\gamma$  channels where further nucleation events can take place.

## 5. Summary and conclusions

This paper presents a detailed investigation of multimodal size distribution of  $\gamma'$  precipitates developing in nickel base superalloys as a result of the phenomenon of multiple  $\gamma'$  nucleation bursts during continuous cooling of the alloy from above the  $\gamma'$  solvus temperature. The salient and novel findings of this paper can be summarized as follows:

1. This paper presents direct evidence of multiple  $\gamma'$  nucleation bursts during continuous cooling based on in situ synchrotron-based X-ray diffraction results where these nucleation bursts have been captured in real time.
2. Coupling multiple characterization techniques – SEM, EFTEM and APT – the size distribution of three distinct populations of  $\gamma'$  precipitates, resulting from these nucleation bursts, have been quantified.
3. The experimental evidence, based primarily on APT investigations coupled with energy-filtered TEM studies, clearly reveals the coupled thermodynamic and kinetic (diffusion) rationale for the formation of  $\gamma'$ -depleted precipitate-free zone adjacent to the first generation of  $\gamma'$  precipitates formed. Thus, while local compositional equilibrium is achieved near the  $\gamma'/\gamma$  interface of these first-generation precipitates, the continuous cooling process does not permit the longer-range far-field  $\gamma$  composition to equilibrate, leading to a higher supersaturation in the matrix at lower temperatures, and eventually resulting in the next nucleation burst. This explanation is a direct experimental validation of the phase-field models discussed previously.
4. Based on the experimental evidence presented in this paper, the rationale for the formation of a third generation of  $\gamma'$  precipitates in between the first and second generations of precipitates has been clearly explained.
5. The experimental results lead to some fundamental questions regarding the differences in the precipitation mechanisms of first-generation  $\gamma'$  precipitates (at lower undercooling or higher temperature) vs. the second or third generation of  $\gamma'$  precipitates (at higher undercooling or lower temperature). Thus, while the first generation of precipitates appears to follow a classical nucleation and growth pathway, the second (or third) generation of precipitates exhibits features of a far-from-equilibrium non-classical mechanism of precipitation. On formation, these second- (or third-) generation precipitates exhibit far-from-equilibrium compositions and compositionally diffuse  $\gamma'/\gamma$  interfaces with large widths.
6. Isothermal annealing of the continuously cooled alloy at 760 °C results in the compositional equilibration of both  $\gamma'$  precipitates as well as the  $\gamma$  matrix and the long-range non-equilibrium diffusion profiles are obviated.

Future studies will involve a more detailed investigation of the formation mechanism of second- or third-generation  $\gamma'$  precipitates in these alloys, that typically form at high undercooling (low temperature) and could therefore exhibit far-from-equilibrium non-classical precipitation behavior. Such non-classical characteristics of the second- or third-generation precipitates can have a significant impact on the nature of the  $\gamma'/\gamma$  interface, which in turn directly impacts on the high temperature microstructural stability (coarsening behavior) as well as the mechanical properties of these alloys.

### Acknowledgements

The authors would like to acknowledge the US Air Force Research Laboratory (AFRL ISES contract FA8650-08-C-5226) for providing financial support for this study. In addition, the authors also gratefully acknowledge the Center for Advanced Research and Technology (CART) at the University of North Texas and the Center for the Accelerated Maturation of Materials (CAMP) at the Ohio State University for access to the experimental facilities used for this study. The use of the Advanced Photon Source was supported by the US Department of Energy, Office of Science, and Office of Basic Energy Science under Contract No. DE-AC02-06CH11357.

### References

- [1] Mitchell RJ, Preuss M. Metall Mater Trans A 2007;38:615.
- [2] Reed RC. The superalloys: fundamentals and applications. Cambridge: Cambridge University Press; 2006.
- [3] Krueger DD, Kissinger RD, Menzies RD, Wukusick CS. US Patent 4,957,567.
- [4] Krueger DD, Kissinger RD, Menzies RD. In: Antolovich SD, et al., editors. Superalloys 1992. Warrendale, PA: TMS-AIME; 1992. p. 277.
- [5] Wlodek ST, Kelly M, Alden DA. In: Kissinger RD, Deye DJ, Anton DL, Cetel AD, Nathal MV, Pollock TM, Woodford DA, editors. Superalloys 1996. Warrendale, PA: TMS; 1996. p. 129.
- [6] Babu SS, Miller MK, Vitek JM, David SA. Acta Mater 2001;49:4149.
- [7] Hwang JY, Banerjee R, Tiley J, Srinivasan R, Viswanathan GB, Fraser HL. Metall Mater Trans A 2008;40:24.
- [8] Seidman DN, Sudbrack CK, Yoon KE. JOM 2006;58:34.
- [9] Sarosi PM, Wang B, Simmons JP, Wang Y, Mills MJ. Scripta Mater 2007;57:767.
- [10] Wen YH, Simmons JP, Shen C, Woodward C, Wang Y. Acta Mater 2003;51:1123.
- [11] Wen YH, Wang B, Simmons JP, Wang Y. Acta Mater 2006;54:2087.
- [12] Radis R, Schaffer M, Albu M, Kothleitner G, Polt P, Kozeschnik E. Acta Mater 2009;57:5739.
- [13] Singh ARP, Nag S, Hwang JY, Viswanathan GB, Tiley J, Srinivasan R, et al. Mater Char 2011;62(9):878.
- [14] Boussinot G, Finel A, Le Bouar Y. Acta Mater 2009;57:921.
- [15] Miller MK. Micron 2001;32:757.
- [16] Blavette D, Cadel E, Deconihout B. Mater Char 2000;44:133.
- [17] Miller MK, Cerezo A, Hetherington MG, Smith GDW. Atom probe field ion microscopy. Oxford: Oxford University Press; 1996. p. 476.
- [18] MacSleay J, Uchic MD, Simmons JP, De Graef M. Acta Mater 2009;57:6251.
- [19] Sarosi PM, Viswanathan GB, Whitis D, Mills MJ. Ultramicroscopy 2005;103:83.
- [20] Little Jr JW, Pettit RG, Schirra JJ, Cowles BA, Holmes RA, Russ SM, et al. Materials damage prognosis. Warrendale, PA: TMS; 2005. p. 23.
- [21] Thompson K, Lawrence D, Larson DJ, Olson JD, Kelly TF, Gorman B. Ultramicroscopy 2007;107:131.
- [22] Tiley J, Srinivasan R, Banerjee R, Viswanathan GB, Toby B, Fraser HL. Mat Sci Technol 2009;25(11):1369.
- [23] Hellman OC, Vandenbroucke JA, Rusing J, Isheim D, Seidman DN. Micro Micro 2000;6:437.
- [24] Cahn JW, Hilliard JE. J Chem Phys 1959;31:688.
- [25] Soffa WA, Laughlin DE. Acta Metall 1989;37:3019.
- [26] Hill SA, Ralph B. Acta Metall 1982;30:2219.
- [27] Laughlin DE. Acta Metall 1976;24:53.
- [28] Viswanathan GB, Banerjee R, Singh A, Nag S, Tiley J, Fraser HL. Scripta Mater 2011;65:485.